Atmospheric boundary layer structure over the Arctic Ocean during MOSAiC

Shijie Peng[1], Qinghua Yang[1], Matthew D. Shupe[2,3],

Xingya Xi[1], Bo Han[1], Dake Chen[1], Changwei Liu[1*]

1 School of Atmospheric Sciences, Sun Yat-sen University, and Southern Marine Science and Engineering

Guangdong Laboratory (Zhuhai), Zhuhai 519082, China

2 Cooperative Institute for the Research in Environmental Science, University of Colorado Boulder, Boulder, CO,

USA

3 NOAA Physical Science Laboratory, Boulder, CO, USA

Correspondence to: Changwei Liu (liuchw8@mail.sysu.edu.cn)

Abstract

The important roles of the atmospheric boundary layer (ABL) over the Arctic Ocean in the Arctic climate system have been recognized, but the atmospheric boundary layer height (ABLH), as a fundamental variable to characterize the vertical structure of ABL, has rarely been investigated. Analyzing a year-round radiosonde dataset during the Multidisciplinary drifting Observatory for the Study of Arctic Climate (MOSAiC), we suggest the optimal critical value of 0.15 of bulk Richardson number to derive ABLH. Based on this algorithm, the hourly ABLH values are derived to analyze the characteristics and variability of ABLH over the Arctic Ocean. The results reveal that the annual cycle is clearly characterized by a distinct peak in May and an abrupt decrease in the following July and August, with a second minimum in December and January. The annual ABLH variation is primarily controlled by the evolution of ABL thermal structure. The temperature inversions in the winter and summer are intensified by seasonal radiative cooling and surface melting, respectively, leading to the low ABLH. The near-surface conditions can also play a significant role in ABLH variation, with turbulent parameters (e.g., friction velocity and turbulent dissipation rate) well correlated with the ABL development. In addition, the MOSAiC ABLH is more suppressed than the ABLH during the Surface Heat Budget of the Arctic Ocean (SHEBA) experiment in the summer, which indicates that there is large variability in the Arctic ABL structure during summer melting season.

30

1 Introduction

31   In recent years, rapidly changing climate and declining sea ice in the Arctic has been reported

32   by numerous studies (Kwok, 2018; Hartfield et al., 2018). The Arctic near-surface temperature is

33   increasing at a rate 2–3 times larger than the global average, which is referred to as Arctic

34   amplification (Overland et al., 2019; Blunden and Arndt, 2019), and the Arctic has entered the 'new

35   Arctic' period (Landrum and Holland, 2020). As a key component of the Arctic climate system and

36   the essential place for atmosphere-ice-ocean interactions, the atmospheric boundary layer (ABL)

37   over the Arctic Ocean is closely associated with Arctic warming and has a big impact on sea ice loss

38   (Francis and Hunter, 2006; Graversen et al., 2008; Wetzel and Bruemmer, 2011). Thus, it is critical

39   to improve our understanding of Arctic ABL processes under 'new Arctic' conditions.

40   The ABL structure over the Arctic Ocean has unique characteristics due to the presence of

41   semipermanent sea ice, and involves various mechanisms and interactions with the surface.

42   Currently, most studies of the Arctic ABL structure are mainly based on coastal observatories and

43   limited drifting ice stations (Knudsen et al., 2018; Vullers et al., 2021). It is found that the

44   predominant temperature inversion in the lower troposphere exists in all seasons and is referred to

45   as the "Arctic inversion" (Andreas et al., 2000; Tjernström et al., 2009). During summer, the Arctic

46   inversion is sometimes elevated, and near-neutral stability occurs below the inversion (Persson et

47   al., 2002; Tjernström et al., 2012). The Arctic vertical structure is influenced by many factors, such

48   as warm-air advection, surface melt, and cloud-top cooling (Busch et al., 1982; Vihma et al., 2011;

49   Vihma, 2014). Investigations of the ABL structure evolution and its controlling factors are the keys

50   to knowing the ABL's role in the Arctic atmosphere.

51   Atmospheric boundary layer height (ABLH) is the key indicator of the ABL structure, referred

52   to as top height of the ABL (Seibert et al., 2000; Seidel et al., 2012). It determines the vertical extent

53   of many atmospheric processes, such as turbulent mixing, convective transport, and aerosol

54   distributions, and is an important parameter for weather and climate models (Deardorff, 1972;

55   Suarez et al., 1983; Holtslag and Nieuwstadt, 1986). In some previous literature, the ABLH over the

56   Arctic Ocean is usually defined as the height of the surfaced-based inversion top or the capping

57   inversion base (e.g., Tjernström et al., 2009; Sotiropoulou et al., 2014). However, as the most

58   fundamental characteristic of the ABL, the turbulence is not fully considered in this definition. There

60　are two forms of turbulent mixing in the Arctic atmosphere. First, the surface mixed layer, formed

61　by turbulent mixing processes near the surface, is frequently shallower than the Arctic inversion

62　layer (Mahrt, 1981; Andreas et al., 2000). Second, the turbulence in low-level clouds, which is

63　driven by radiative cooling near the cloud top, forms a cloud-induced mixed layer (Solomon et al.,

64　2011; Shupe et al., 2013). This cloud mixed layer is sometimes decoupled from the surface mixed

65　layer while at other times it extends down to form a coupled, well-mixed layer all the way to the

66　surface (Shupe et al., 2013; Brooks et al., 2017). Based on the turbulence characteristics, the ABLH

67　is commonly determined by the profiles of potential temperature, wind speed, and humidity, and

68　various ABLH determination methods have been proposed (Seibert et al., 2000; Seidel et al., 2010).

69　However, the applicability of these methods in the Arctic needs to be further validated.

70　　　Due to the lack of observations, there are few analyses of ABLH over the Arctic Ocean based

71　on observational data. The distributions of Arctic ABLH are preliminarily investigated by

72　Tjernström and Graversen (2009), Liang and Liu (2010), and Dai et al. (2011), but their studies are

73　all based on the Surface Heat Budget of the Arctic Ocean (SHEBA) campaign conducted 20 years

74　ago (Uttal et al., 2002). We need more comprehensive and new observations to improve our

75　understanding of the ABL structure and ABLH characteristics under "new Arctic" conditions. The

76　Multidisciplinary drifting Observatory for the Study of Arctic Climate (MOSAiC) expedition was

77　especially designed to achieve this goal (Shupe et al., 2022). By drifting a research vessel in the

78　central Arctic for a whole year, the MOSAiC expedition carried out numerous observing activities.

79　It provided a wealth of data and related data products with unprecedented high temporal resolution

80　and year-round temporal coverage. These data make possible a more detailed analysis of the ABL

81　structure evolution and ABLH variability.

82　　　In this study, based on observational data from the MOSAiC expedition, we propose an ABLH

83　calculation algorithm and reveal the characteristics of the ABL evolution over the Arctic sea-ice

84　surface in the 'new Arctic'. This paper is organized as follows: section 2 briefly describes the

85　MOSAiC expedition and the observations; section 3 provides an ABLH determination method to

86　evaluate several automated algorithms, and develops the optimal ABLH algorithm; section 4

87　presents the results of ABLH variation over the annual cycle, the controlling factors of ABLH

88　variation, and mechanisms of ABL development and suppression; discussion and conclusions are

89　given in section 5 and section 6, respectively.

90

2 Measurements

The MOSAiC expedition track is shown in Fig. 1, which is based on the research vessel *Polarstern* (Knust, 2017), with the main period of atmospheric state observations starting in October 2019 and ending in September 2020. *Polarstern* drifted across the central Arctic Ocean and navigated through the ice floes north of 80° N during most of the MOSAiC year. The whole drifting period is divided into five parts, and the vessel sailed in the gap period between some of those parts. More details are described in Shupe et al. (2022). The following are the descriptions of the instruments and data products used in this paper.

2.1 Radiosonde observations and retrieval product

The radiosonde program was undertaken by the Alfred Wegener Institute (AWI) and the US Department of Energy Atmospheric Radiation Measurement Program (DOE-ARM), and the data are publicly available on the PANGAEA archive (Maturilli et al., 2021). Radiosondes were regularly launched on board throughout the whole MOSAiC year (from October 2019 to September 2020), including periods when the vessel was in transit. The sounding frequency is normally four times per day (launched at about 5:00, 11:00, 17:00, and 23:00 UTC) and is increased to 7 times per day during the special periods of exceptional weather or coordination with other observing activities. The radiosoundings provide fundamental data of the atmospheric state, including vertical profiles of pressure, temperature, relative humidity, and winds, over the altitude range of 12 m up to 30 km. In addition, DOE-ARM also provides a Planetary Boundary Layer Height Value-Added Product (PBLHT VAP, Riihimaki et al., 2019). The VAP contains virtual potential temperature, potential temperature gradient, Richardson number, and other parameters derived from radiosonde data, as well as estimates of the ABLH by using several different automated algorithms. In this paper, data quality control and a six-point moving average in height are applied to raw radiosonde data to eliminate invalid data and measurement noise, and all data are interpolated onto a regular vertical grid with 10 m intervals. Moreover, we cut off the sounding data observed below 100 m altitude considering the potential contamination of the vessel itself.
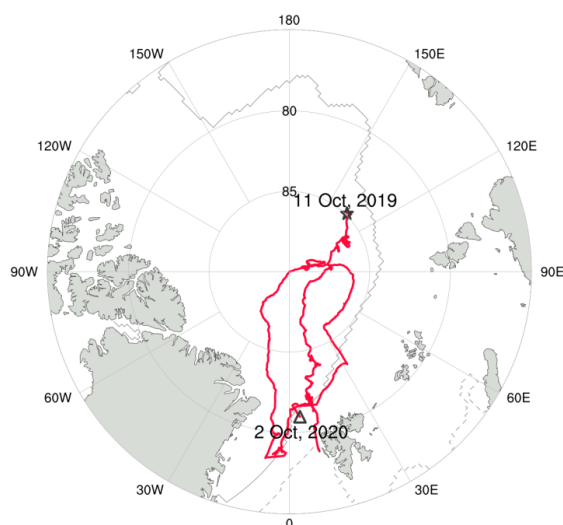
119

120 Figure 1 The MOSAiC expedition track from (star) 11 October 2019 through to (triangle) 2 October

121 2020 is plotted by the red line. Gray solid and dashed lines denote the approximate sea ice edge at

122 the minimum (15 September 2020) and the maximum (5 March 2020), respectively.

123

124 **2.2 Interpolated sounding value-added product**

125 In order to further analyze the characteristics of ABLH during the MOSAiC expedition, the

126 Interpolated Sounding Value-Added Product (Jensen et al., 2019) is used in our study. The VAP,

127 which is also provided by DOE-ARM, transforms routine atmospheric state data into continuous

128 time-height gridded data, with a 1 min time resolution and 20 m height resolution. The input data

129 come from multiple source instruments, including radiosondes, ceilometers, micropulse lidar, and

130 others, all installed on Polarstern. All meteorological variables are linearly interpolated onto the

131 fixed grid. Relative humidity is corrected with the microwave radiometer-derived precipitable water

132 vapor column. The time range of the VAP is the same as that of radiosonde observations, covering

133 the whole MOSAiC expedition (from October 2019 to September 2020). In this paper, atmospheric

134 temperature, moisture, pressure, and horizontal wind in the VAP are used and processed into hourly

135 averaged data for analysis.

136

137 **2.3 Meteorological and turbulence measurements near the surface**

138 Meteorological and turbulence measurements were made from a tower on the sea ice at "Met

139   City", which was located 300–600 m away from the vessel. The u-Sonic-3 Cage MP anemometers

140   by METEK GmbH and air temperature sensors HMT330 by Vaisala were fixed at nominal heights

141   of 2 m, 6 m, and 10 m on the meteorological tower. The tower was set up during the periods when

142   the vessel drifted with an ice floe (i.e., from mid-October 2019 to mid-May 2020, from mid-June to

143   July 2020, and from late August to mid-September 2020). The sampling frequency of fast response

144   instruments (i.e., u-Sonic-3 Cage MP anemometer) was at 20 Hz, resampled to 10 Hz. To derive

145   turbulence parameters, the following processes were carried out: despiking, block averaging over a

146   10-min interval, coordinate rotating via double rotation, frequency correcting, and virtual

147   temperature correcting (Cox et al., 2023). In this study, sensible heat flux (SH, defined as positive

148   upwards), near-surface air temperatures at the heights of 2 m and 10 m, friction velocity, and

149   turbulent kinetic energy (TKE) dissipation rate are used and processed into hourly-averaged data,

150   consistent with the time resolution of Interpolated Soundings. We neglect the distance between the

151   vessel and "Met City" and consider that their ABL conditions are the same, particularly when

152   considered on hourly timescales.

153

3 ABLH determination method and algorithm evaluation

155   The most objective method of ABLH determination is based on profiles of turbulence

156   measurements deployed on aircraft or other platforms, but such measurements were not routinely

157   carried out during the MOSAiC expedition. Thus, the ABLH determination in our study is based on

158   the thermal and dynamic structure of radiosoundings. In previous literature, the ABLH is determined

159   through multiple profiles of atmospheric variables and manual visual inspection, which is usually

160   conducted with small data volume and can be seen as the "observed" ABLH (Liang and Liu, 2010;

161   Zhang et al., 2014; Jozef et al., 2022). In this section, we will describe the subjective ABLH

162   determination method and obtain the ABLH using the radiosonde profiles. Next, we will use these

163   ABLHs as observed values to evaluate the automated ABLH algorithms provided by the VAP.

164   Finally, we will find the optimal ABLH automated algorithm for subsequent calculations of high-

165   resolution results.

166

3.1 ABLH determination method

168   The ABLH determination method starts with the classification of ABL regimes. Considering the

169 unique structure of the Arctic ABL, we divide the ABLs into two types: stable boundary layer (SBL)

170 and convective boundary layer (CBL), corresponding with stable stratification or a well-mixed layer

171 with unstable conditions in the lower troposphere, respectively. Based on previous studies (e.g.,

172 Vogelezang and Holtslag, 1996; Liang and Liu, 2010), *SH* and potential temperature profiles are

173 used to diagnose the ABL regime types, representing the surface conditions and the atmospheric

174 stability, respectively. If the potential temperature difference between the 150 and 100 m heights is

175 less than a critical value, and *SH* is larger than 0, then the ABL is identified as a CBL. Otherwise,

176 the ABL is identified as a SBL. The specific classification formula is presented below:

177
$$\begin{cases} \theta_{150m} - \theta_{100m} \leq \delta_s \ and \ SH > 0 & \text{for CBL} \\ else & \text{for SBL} \end{cases} \tag{1}$$

178 where θ is potential temperature, and its subscript denotes the height considered ; δ_s is the

179 critical value, which is primarily dependent on surface characteristics. Based on the thermodynamic

180 properties of the ocean and sea ice surface of the Arctic Ocean, the value of δ_s is specified as 0.2 K

181 (Liang and Liu, 2010).

182 The subjective ABLH determination in our study is based on characteristics of sounding profiles

183 and regime types. For each atmospheric sounding profile, potential temperature (θ), potential

184 temperature gradient (θ_{grad}), wind speed (WS), specific humidity (q_v), and relative humidity (RH)

185 are used to obtain multiple estimates of the ABLH, and the observed ABLH is determined through

186 these estimates. Two cases to describe the method are presented in Fig. 2. Figures 2 (a–c) are the

187 case of a SBL, which features a surface temperature inversion and surface humidity inversion. For

188 this SBL, the estimates of the ABLH are defined as the level at which the θ_{grad} and the WS reach

189 the maximum, and the RH rapidly decreases. Figures 2 (d–f) are the case of a CBL, with

190 approximately constant θ from the surface up to the inversion base and low-level cloud coupled to

191 the surface (e.g., Shupe et al., 2013). For a CBL, the ABLH estimate based on WS is the same as

192 that used for a SBL, whereas based on profiles of potential temperature and humidity, the ABLH

193 estimates are defined as the base of the θ inversion and the base of the q_v inversion, respectively.

194 Subsequently, based on these estimates, the observed ABLHs (solid black line in Fig. 2) are

195 determined through manual identification. The specific rules of manual identification are as follows:

196 (1) If the estimates differ slightly from each other, take the average of these estimates as ABLH; (2)

197 If a strong characteristic (sharp gradients or peaks) of the profile is evident, select the estimate

198   obtained based on this characteristic; (3) If the ABL structure was similar to that at the previous

199   time, select the estimate with the smallest change to ensure that ABLHs are consistent in time; (4)

200   If the estimates differ greatly and ABLH determination is difficult, the ABLH at the time is identified

201   as missing value and excluded from further analysis; In total, we select 686 samples from 964

202   radiosonde profiles, and all data from observations while the vessel was in transit have been

203   excluded. Using multiple estimates as references and excluding unconfident values can make the

204   ABLH determination more reliable.

205
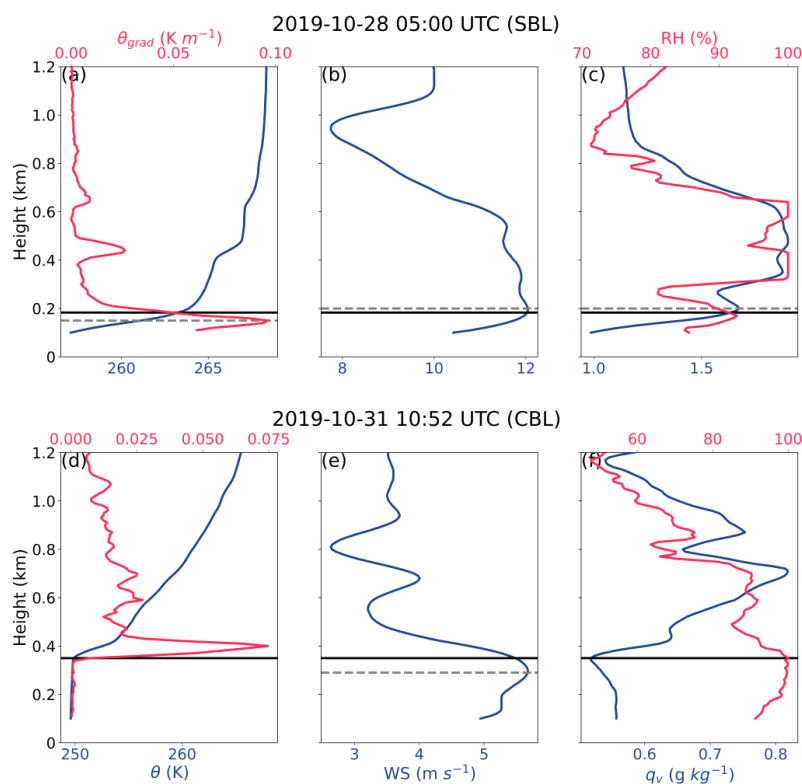
206   Figure 2 Vertical profiles of (left) potential temperature (θ), potential temperature gradients

207   (θ_{grad}), (middle) wind speed (WS), and (right) relative humidity (RH) and specific humidity (q_v)

208   at (a–c) 28 October 2019, 05:00 UTC and (d–f) 31 October 2019, 10:52 UTC. Boundary layers at

209   the two times represent stable boundary layer (SBL) and convective boundary layer (CBL),

210   respectively. The gray dashed horizontal lines denote the atmospheric boundary layer height (ABLH)

211   estimates based on multiple methods, and the black solid horizontal lines denote the manually

212   observed ABLHs.

213

3.2 Automated algorithms evaluation

The automated ABLH algorithms consist of various empirical formulas. Based on these empirical formulas, estimated ABLHs are determined automatically and without manual intervention. Therefore, these algorithms can perform real-time and fast calculations on large amounts of data and are widely used in model simulations (Seibert et al., 2000; Konor et al., 2009). However, automated algorithms might lead to large errors in estimating ABLHs, and the parameter selection in algorithms will also have a great impact on the results. In our study, estimated ABLHs obtained using three automated algorithms are compared with subjective ABLHs to evaluate their performance in the Arctic Ocean. These algorithms, including the Liu-Liang algorithm, the Heffter algorithm, and the bulk Richardson number algorithm, are all applied in the PBLH VAP. Here we give a brief description of the three algorithms.

The Liu-Liang algorithm determines ABLH based on potential temperature and wind speed. For CBL regimes, the definition of ABLH is the height at "which an air parcel rising adiabatically from the surface becomes neutrally buoyant". For SBL regimes, two different estimates of the SBL height are obtained based on stability criteria and wind shear criteria, respectively. Then the SBL height is usually defined as the lower of the two heights. More details for the Liu-Liang algorithm are described in Liang and Liu (2010).

The Heffter algorithm, which was suggested by Heffter (1980), is a widely used algorithm (e.g., Marsik et al., 1995; Snyder and Strawbridge, 2004). The algorithm determines ABLH through the strength of an inversion and potential temperature difference across the inversion. The ABLH is defined as the lowest layer in which the potential temperature difference between the top and the bottom of the inversion is greater than 2 K. If no layer meets the criteria, the ABLH is defined as the layer at which the potential temperature gradient reaches the largest maximum.

The bulk Richardson number algorithm is based on the profile of the bulk Richardson number (Ri_b), which has been proved to be a reliable algorithm for determining ABLHs (Seidel et al., 2012). Ri_b is a dimensional number that represents the ratio of thermally produced turbulence to that induced by mechanical shear. According to Jens Havskov et al. (1998), Ri_b is expressed as

$$Ri_b = \left(\frac{gz}{\theta_{v0}}\right)\left(\frac{\theta_{vz}-\theta_{v0}}{u_z{}^2+v_z{}^2}\right), (2)$$

242   where g is the acceleration of gravity; θ_{vz} and θ_{v0} are the virtual potential temperature at height

243   z and the surface, respectively; u_z and v_z are the horizontal wind speed component at height z. The

244   ABLH is defined as the height of Ri_b exceeding a critical threshold (the critical bulk Richardson

245   number, Ri_{bc}; Seibert et al., 2000). The PBLH VAP includes ABLH estimates based on two widely

246   used Ri_{bc} values: 0.25 and 0.5.

247   In order to quantitatively evaluate the performance of each automatic algorithm, we introduce

248   the correlation coefficient R and three other statistical measures (Gao et al., 2004). Their calculation

249   formulas are as follows:

250
$$Bias = \frac{\sum_{i=1}^{n}|H_{auto}-H_{obs}|}{n}, (3)$$

251
$$SEE = \sqrt{\frac{\sum_{i=1}^{n}|H_{auto}-H_{obs}|^2}{n-2}}, (4)$$

252
$$NSEE = \sqrt{\frac{\sum_{i=1}^{n}(H_{auto}-H_{obs})^2}{\sum_{i=1}^{n}(H_{obs})^2}}, (5)$$

253   where H_{auto} is the ABLH obtained by the automated algorithm; H_{obs} is the ABLH manually

254   determined; n is the number of valid sounding profile samples; $Bias$ is the absolute bias; SEE is the

255   standard error; and $NSEE$ is the normalized standard error, denoting the relative uncertainty.

256   According to the definitions of these statistical measures, larger R and smaller $Bias$, SEE, and

257    $NSEE$ mean better performance of the automated algorithm.

258   Figure 3 presents the comparisons of estimated ABLHs obtained through the Ri_b algorithm with

259   Ri_{bc} of 0.25, the Ri_b algorithm with Ri_{bc} of 0.5, the Heffter algorithm, and the Liu-Liang algorithm

260   with the subjective ABLHs. The scatter plots show that the ABLHs computed with the Ri_b

261   algorithm with Ri_{bc} of 0.25 agree well with the manual ABLHs in general while they show

262   underestimations for a few CBL samples, indicating that the Ri_b algorithm with Ri_{bc} of 0.25 may

263   be challenged by some CBL conditions. The performance of the Ri_b algorithm with Ri_{bc} of 0.5 is

264   poorer than that of the Ri_b algorithm with Ri_{bc} of 0.25, with overestimations of ABLHs in general,

265   and underestimations for some CBL cases. The Heffter algorithm performs well in cases of high

266   ABLH and particularly for CBL cases, while significant overestimations occur in some cases. This

267   is attributed to the determination criterion of the Heffter algorithm, i.e., ABLHs are determined by

268   inversion layers, which means that large errors occur when the inversion layer is higher than the

269   mixed layer. The performance of the Liu-Liang algorithm is poorer than the other algorithms, which

270   is probably due to the impact of noise in the lower ABLH profiles and unsuitable parameters in the

271   algorithm. In terms of the statistical measures, the ABLHs computed by the Ri_b algorithm with Ri_{bc}

272   of 0.25 show the highest correlations with the H_{obs} with a correlation coefficient of 0.68, and the

273    $Bias$, SEE, and $NSEE$ of the algorithm are also the minima compared with the other approaches.

274   In summary, the Ri_b algorithm is reliable over the Arctic Ocean and performs better than other

275   algorithms, and this result is consistent with Jozef et al. (2022). Furthermore, we will explore the

276   optimal Ri_b algorithm for the Arctic Ocean.

277
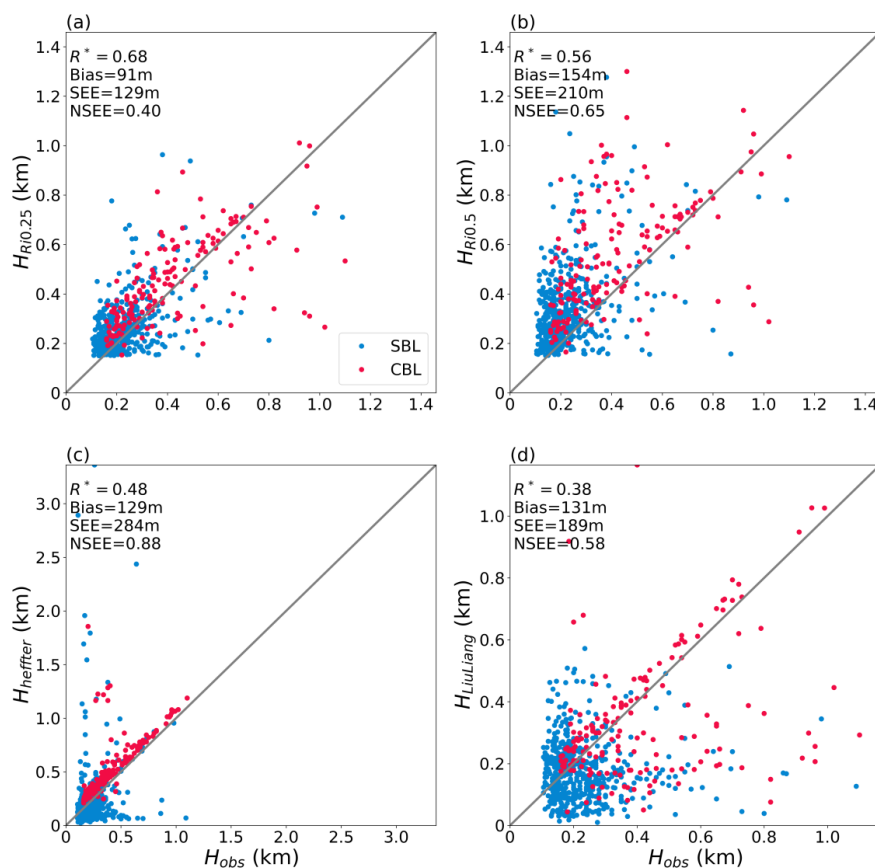
278

279   Figure 3 Comparisons of the ABLHs determined by the bulk Richardson number (Ri_b) algorithms

280   with the critical values (Ri_{bc}) of (a) 0.25 and (b) 0.5, (c) the Heffter algorithm, and (d) the Liu-Liang

281   algorithm and observed ABLHs. The blue and red dots indicate regime types of SBL and CBL,

282   respectively. The correlation coefficient (R), the absolute bias ($Bias$), the standard error (SEE), and

283   the normalized standard error ($NSEE$) are given in each panel. The correlation coefficients with star

284 superscripts indicate that the values are statistically significant ($p < 0.05$).

285

3.3 The Ri_b algorithm with optimal Ri_{bc}

287 In the Ri_b algorithm, the Ri_{bc} is a key indicator to diagnose whether the turbulence flow exists

288 or not. When Ri_b is smaller than Ri_{bc}, a laminar flow starts to become turbulent (Stull, 1988). As

289 can be seen from the above comparisons of the Ri_b algorithm, the value of Ri_{bc} can have a large

290 impact on the estimated ABLH. Although some studies suggest that the Ri_{bc} varies depending on

291 atmospheric stability (Richardson et al., 2013) and is impacted by the hysteresis phenomenon (Banta

292 et al., 2003; Tjernström et al., 2009), the Ri_b algorithm with fixed Ri_{bc} is still often used in many

293 studies (Brooks et al., 2017; Jozef et al., 2022) and numerical models (e.g., Community Climate

294 Model version 2). Likewise, we will adopt the Ri_b algorithm with fixed Ri_{bc} for simplicity, and try

295 to find the best choice of Ri_{bc} for the ABL over the Arctic Ocean during MOSAiC.

296 In the nocturnal strongly SBL and weakly SBL, the range of Ri_{bc} is 0.16–0.22 and 0.23–0.32,

297 respectively (Vogelezang and Holtslag, 1996). For the CBL, the value of Ri_{bc} should be larger than

298 0.25 (Zhang et al., 2011). In our study, we take 0.1–0.5 as the approximate range of Ri_{bc}, and select

299 values at intervals of 0.05 to calculate the ABLHs. Then, the statistical measures are used in

300 comparisons between these estimated ABLHs and manual ABLHs. The results are shown in Table

301 1. When the Ri_{bc} is 0.15, the error is the smallest for all statistical metrics (R, $Bias$, SEE, and $NSEE$

302 are 0.71, 76 m, 115 m, and 0.35, respectively). This result is distinct from that of Jozef et al. (2022).

303 We think the reason might be that our formula of Ri_b, which is provided by the PBLH VAP, is

304 different from theirs, and the result is also sensitive to the vertical resolution of profiles (Dai et al.,

305 2014). We are confident that the Ri_b algorithm with Ri_{bc} of 0.15 is applicable to the data used in

306 our study, and we will use it as the improved Ri_b algorithm for subsequent analysis.

307

308 Table 1 The statistical measures (R, $Bias$, SEE, and $NSEE$) for the Ri_b algorithm with Ri_{bc} of

309 0.10–0.50. The optimal Ri_{bc} and the smallest statistical errors are presented in bold. All correlation

310 coefficients are statistically significant ($p < 0.05$)

Ri_{bc}	R	$Bias$ (m)	SEE (m)	$NSEE$
0.10	0.69	78	118	0.36
0.15	**0.71**	**76**	**115**	**0.35**

0.20	0.70	81	119	0.37
0.25	0.68	91	129	0.40
0.30	0.66	102	143	0.44
0.35	0.61	117	163	0.50
0.40	0.59	130	179	0.55
0.45	0.57	142	196	0.60
0.50	0.56	154	210	0.65

311

312 **4 Results and discussion**

313   **4.1 Overall distribution of ABLH during the MOSAiC expedition**

314   To obtain the ABLH with high temporal resolution, the Interpolated Sounding VAP is used to

315 determine the ABLH based on the Ri_b algorithm with the optimal Ri_{bc} of 0.15, and the ABL type is

316 determined through θ gradient and SH based on Eq. (1), or only θ gradient if SH is unavailable. The

317 full-time series of ABLH during the MOSAiC expedition is presented in Fig. 4. Note that the grey

318 dots indicate that the ABL data was observed while the vessel was in transit. Overall, the mean and

319 95th percentile ABLH during the whole observation period are 228 and 610 m, respectively. This is

320 typically lower than the ABLH over the Arctic land surface (Liang and Liu, 2010), which is

321 primarily attributed to the stronger suppression of the temperature inversion over the sea-ice surface.

322 According to the surface state, the whole MOSAiC observation period is divided into "freeze up",

323 "winter", "transition", and "summer melt" periods (Shupe et al., 2022), roughly corresponding to

324 the seasons of autumn, winter, spring, and summer, respectively. As shown in Fig. 4, the Arctic ABL

325 is suppressed in the stable stratification state for most of the MOSAiC year, while for a few periods

326 it rapidly develops to a height of more than 610 m (95th percentile ABLH), and maintains this height

327 for several days, when the CBL is dominant. For instance, the intensive development of the ABL

328 occurs in the "transition" period from 13 April through to 24 May 2020. In this period, the

329 convectively thermal structure contributes to ABLH reaching over 610 m for about 6 days, with the

330 maximum ABLH of 1152 m. In contrast, the ABL is severely suppressed in the period from 15 July

331 through to 30 August 2020, with the mean ABLH of only 134 m. The specific mechanisms of ABL

332 development and suppression in these two cases will be analyzed as case studies in Sect. 4.3 and

333 Sect. 4.4, respectively.

334   Figure 5 presents the frequency distribution of ABLH under convective and stable regimes.

335   The bin widths of CBL and SBL are 65 m and 45 m, respectively. Overall, the sample number of

336   SBL cases is more than that of CBL cases during the MOSAiC period (72 % for SBL and 28 % for

337   CBL). The distribution of SBL height is narrow, with 69 % of the ABLH lower than 200 m, 97 %

338   of the ABLH lower than 400 m, and a median value of merely 148 m. For CBL, the ABLH

339   distribution has a broader range, with 85 % of the ABLH lower than 600 m and a median value of

340   362 m.

341
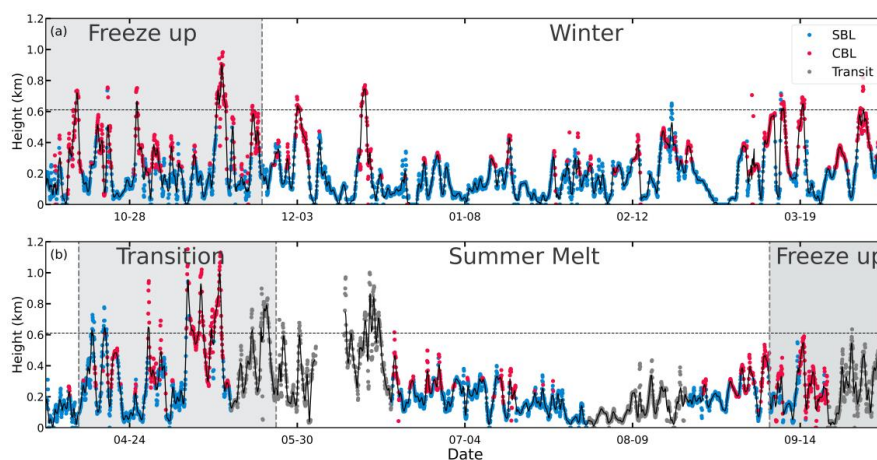
342

343   Figure 4 Time series of ABLHs computed by the optimal Ri_b algorithm throughout the MOSAiC

344   year is divided into (a) and (b). The blue and red dots indicate SBL and CBL, respectively. The gray

345   dots indicate ABL data observed while the vessel was in transit. The black solid line indicates the

346   12-points moving averaged ABLH. The gray dashed horizontal line denotes the 95th percentile of

347   ABLH. The gray and white background shadings indicate the periods under different surface-

348   melting states, i.e., "freeze up", "winter", "transition", and "summer melt" periods.
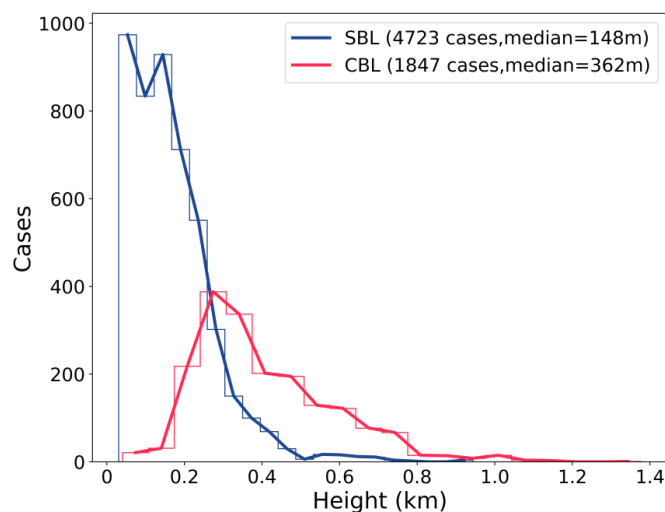
349

350 Figure 5 Frequency distribution of SBL height (blue) and CBL height (red). The case numbers and

351 the median values of ABLH for SBL and CBL are also given.

352

353 **4.2 Annual cycle of ABLH and related factors**

354   Figure 6 presents the annual cycle of monthly ABLH statistics during the MOSAiC expedition

355 in terms of 1st, 25th, 50th, 75th, and 99th percentiles of ABLH (boxplots) and the mean value ("x"

356 signs and colored solid lines). The results show a distinct peak in May, with a median value of 345

357 m and the 99th percentile reaching over 1000 m. An abrupt decrease occurs in the following July

358 and August, and another minimum occurs in December and January, all with median values around

359 150 m. In terms of different regime types, the annual cycle of ABLH for both SBL and CBL follow

360 a similar pattern. However, the SBL cases show an annual minimum in October while the CBL

361 cases show an annual minimum in August. We use this result to compare with the ABLH distribution

362 during the SHEBA period according to Dai et al. (2011). In Sect. 5, we will discuss the differences

363 and possible reasons.

364   The annual cycle of ABLH is determined by the seasonal evolution of the ABL structure

365 (Tjernström et al., 2009; Palo et al., 2017). The median profiles of equivalent potential temperature

366 (θ_E) in each month are presented in Fig. 7 to investigate the determining factors of the annual cycle

367 of ABLH. The results show that from the start of the MOSAiC expedition (October 2019), the near-

368 surface θ_E gradually decreases due to seasonal surface radiative cooling in the absence of sunlight,

369   more rapidly than the atmosphere cools, which causes a strong surface temperature inversion. The

370   increasing inversion strength through January leads to decreasing ABLH into "winter." In February

371   and March, the surface remains steady while the atmosphere cools more, leading to diminished

372   temperature inversion strength and an increase in ABLH. After March 2020, with the return of

373   sunlight, the θ_E starts to rise over the whole lower atmosphere, and the near-surface air temperature

374   warms somewhat more than the atmosphere above. This differential warming leads to near-neutral

375   or convective thermal structure and contributes to high ABLH during the "transition" period. In July

376   and August, the upper-layer temperature continues to rise while the near-surface temperature is

377   constrained to ~0 ℃ due to the melting sea ice surface, which leads again to a surface inversion,

378   corresponding with low ABLH during the "summer melt" period. In September, as the sun descends

379   to much lower angles, the θ_E across the whole lower atmosphere starts to drop, with more rapid

380   cooling in the atmosphere relative to the near-surface resulting again in a near-neutral or convective

381   thermal structure and an increase in the CBL height during the "freeze up" period, which links back

382   to where the annual cycle began.
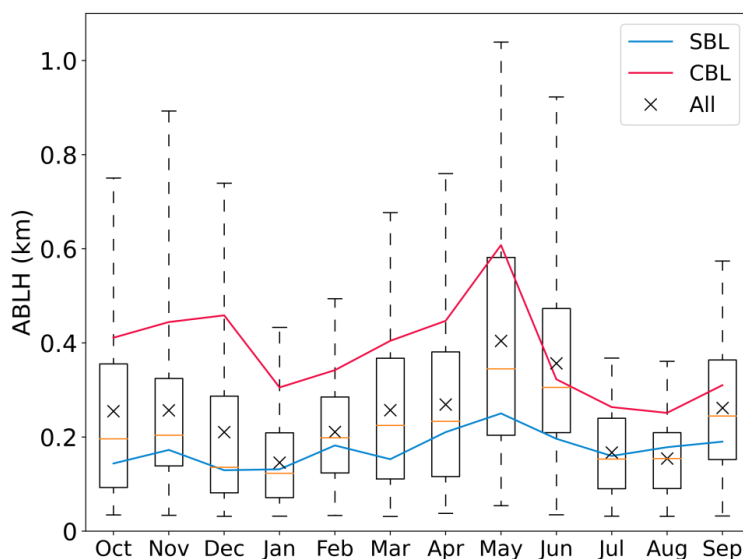
383

384   Figure 6 Box-and-whisker plots of ABLH distribution in each month throughout the MOSAiC year.

385   The whiskers, the boxes, and the yellow horizontal lines show the 1th, 25th, 50th, 75th, and 99th

386   percentile values of ABLH. The blue and red solid lines and the "x" signs indicate the mean ABLH

387   of SBL, CBL, and all regime types, respectively.

388
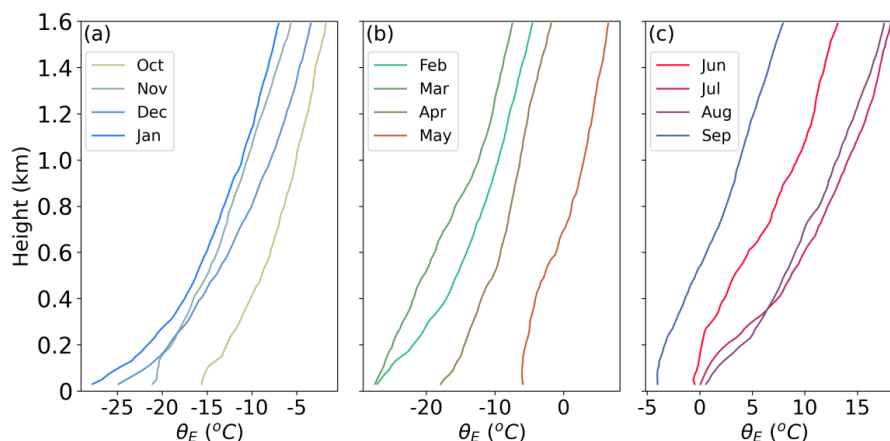
389

390 Figure 7 Median profiles of equivalent potential temperature (θ_E) throughout the MOSAiC year are

391 divided into (a), (b), and (c).

392

393   In order to further explore the surface conditions that influence the ABLH, we evaluate the

394 correlations between the ABLH and three near-surface meteorological and turbulence parameters

395 during the MOSAiC period, including temperature gradient ($T_{grad} = T_{10m} - T_{2m}$), friction velocity

396 (u^*), and TKE dissipation rate (ε). The results are shown in Fig. 8. Generally, T_{grad}, u^*, and ε

397 represent near-surface buoyancy effects, mechanical mixing, and turbulence intensity, respectively.

398 In Fig. 8a, the ABLH distribution for negative T_{grad} has a wide range from the lowest level to above

399 1 km. As T_{grad} becomes positive and increases, the ABLH distribution rapidly narrows to below

400 200 m. In general, positive T_{grad} means a stably stratified ABL and surface-based temperature

401 inversion, both of which lead to low ABLH, and negative T_{grad} means that atmospheric stability

402 near the surface is near-neutral or convective, which is necessary for the ABL development. The u^*

403 presents a significant correlation with the ABLH, with correlation coefficient of 0.65 (Fig. 8b). High

404 u^* values, which are related to strong mechanical mixing, contribute to the ABL development.

405 However, it is worth noting that intensive ABL development (ABLH over 800 m) only occurs as u^*

406 ranges between the 0.2 and 0.5 m s^{-1}, which suggests that other factors exist to facilitate further

407 development of the ABL, such as cloud effects (Tjernström, 2007; Shupe et al., 2013). The ε is

408 usually a qualitative proxy for turbulence intensity, since higher TKE means larger spectral values

409 at low frequencies, hence higher dissipation rate due to the energy cascade in the inertial subrange.

410   In Fig. 8c, as ε is less than $5 \times 10^{-5}\ m^2 s^{-3}$, turbulence in the ABL is limited with almost all ABLH

411   below 200 m. As ε increases and becomes larger than $5 \times 10^{-5}\ m^2 s^{-3}$, the ABLH increases with

412   active turbulent mixing in the ABL. The threshold of $5 \times 10^{-5}\ m^2 s^{-3}$ is accorded by Brooks et al.

413   (2017). In summary, near-surface conditions play a key role in the ABL development and are also

414   an indicator, in that one can roughly determine the development state of the whole ABL from the

415   near-surface conditions alone.

416
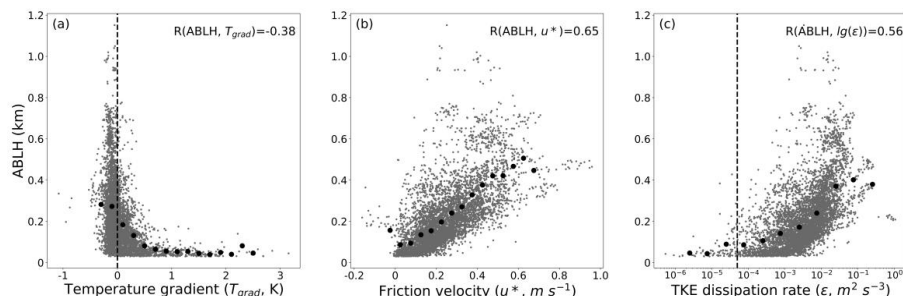
417

418   Figure 8 The ABLHs and bin-averaged values for (a) temperature gradient, T_{grad} (K), (b) friction

419   velocity, u^* (m s^{-1}), and (c) turbulent kinetic energy dissipation rate, ε (m^2 s^{-3}). The average bins for

420   T_{grad}, u^*, and ε logarithm are 0.2 K, 0.05 m s^{-1}, and 0.5 m^2 s^{-3} respectively. The correlation

421   coefficients R are given in each panel, all of which are statistically significant ($p < 0.05$). The dashed

422   vertical lines indicate the thresholds of (a) T_{grad}=0 K and (c) $\varepsilon = 5 \times 10^{-5}\ m^2 s^{-3}$.

423

424   **4.3 Case study #1: Intensively developed ABL**

425   In order to investigate the unique characteristics of the ABL development and its controlling

426   factors in detail, we analyze the association of the ABLH with vertical thermal structure and near-

427   surface conditions during the transition period (see Fig. 4) when the ABLH was generally highest.

428   Figure 9 presents time-height cross sections of θ_E, wind speed, and relative humidity, and the time

429   series of near-surface temperature and surface pressure during this period. We divide the whole

430   period into three parts based on the ABLH and the vertical structure of the lower troposphere.

431   Overall, the near-surface temperature is generally warmer than -20 ℃ and shows gradual warming

432   towards the melting point. In Period 1, a warm and moist air advection event affects the

433   measurement area, resulting in increased air temperature, near-saturated relative humidity, strong

434   winds throughout the lower troposphere, and low surface pressure. The approximately constant θ_E

435   profile near the surface facilitates exchange between the upper and lower layers, and the high-speed

436   wind profile enhances mechanical mixing, leading to highly developed ABL and ABLH exceeding

437   600 m. In Period 2, the air temperature drops again to between -20 and -10 ℃, which causes a

438   temperature inversion and partially suppresses the ABL development. However, the near-saturated

439   relative humidity indicates that the cloud-mixed layer couples with the surface-mixed layer, which

440   facilitates the ABL development. The ABLH is related to the depth of the near-saturated layer,

441   consistent with a structure where the cloud-induced mixed layer couples with the near-surface mixed

442   layer, forming a deeper ABL and higher ABLH (Wang et al., 2001; Shupe et al., 2013). In Period 3,

443   a high-pressure synoptic system occurs and suppresses the development of the ABL, but the cloud-

444   driven turbulent mixing still exists and counteracts the influence of the high-pressure system. In

445   summary, the development of the ABL mainly depends on large-scale synoptic processes, especially

446   warm-air advection events. Additionally, the interaction between the surface-mixed layer and cloud-

447   mixed layer also plays a significant role in the ABL development.

448
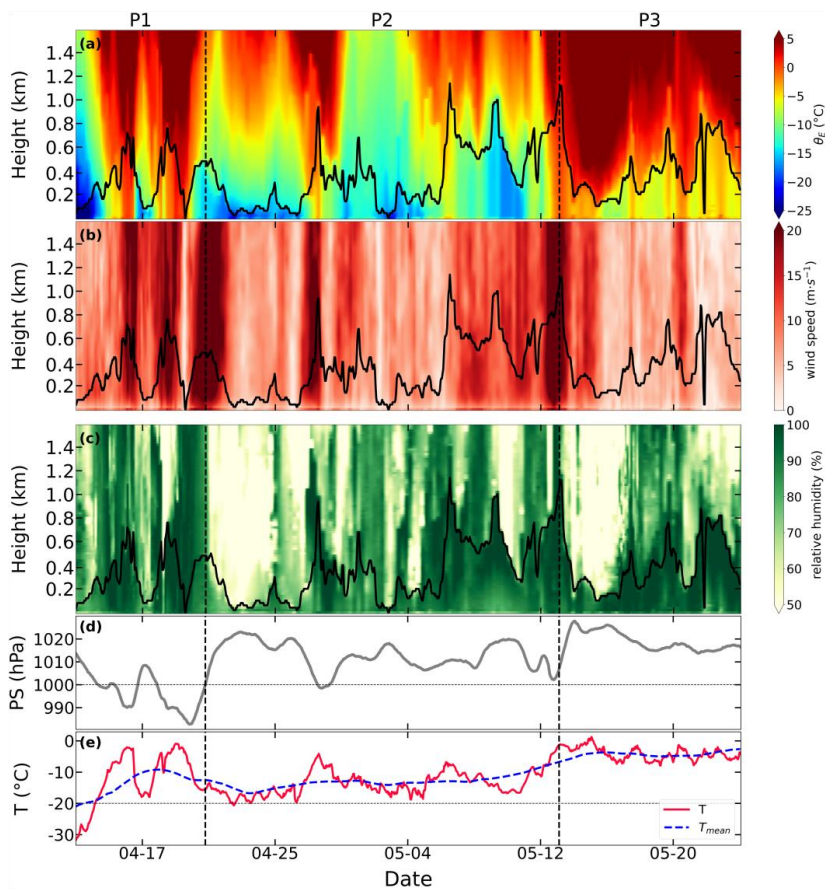
Figure 9 Time-height sections of (a) equivalent potential temperature, (b) wind speed, and (c)
relative humidity and time series of (d) surface pressure and (e) near-surface temperature (red line)
and 7 d running mean of near-surface temperature (blue line). The whole period is from 13 April
2020 to 24 May 2020. Vertical dashed lines mark the identified key periods P1 to P3. The black
solid lines in panels (a–c) denote the ABLH during this period.

4.4 Case study #2: the severely suppressed ABL

The Arctic ABL is suppressed most of the time, especially in the late summer, for more than a
month. We choose the severely suppressed ABL in this period as a case to analyze the influences of
vertical thermal structure and near-surface conditions on the ABLH. The results are shown in Fig.
10, and the whole period is divided into three parts, similar to Fig. 9. In Period 1, the near-surface
air temperature is constrained to ~0 ℃ due to the melting surface, and the temperature inversion and

461 weak wind are dominant throughout the lower troposphere, which suppresses the ABL development.

462 In Period 2, warm-air advection occurs in the lower troposphere, strengthening the temperature

463 inversion and contributing to ABL suppression and an ABLH lower than 100 m. Because of the

464 constrained near-surface temperature, this structure is distinct from that of the "transition" period

465 when warm-air advection facilitates ABL development. In Period 3, the near-surface and upper-

466 layer temperatures start to decrease, and the temperature inversion weakens, which makes the ABLH

467 periodically grow up to ~400 m. Despite that, the ABL is still stably stratified, and the decoupled

468 cloud-mixed layer aloft does not interact with the near-surface environment, in part due to different

469 θ_E in each layer, which is consistent with Shupe et al. (2013). In summary, the suppression of the

470 ABL during the "summer melt" period results from strong temperature inversions and weak winds,

471 and cloud-driven turbulent mixing that does not interact with the surface layer. In this period, warm-

472 air advection events enhance the ABL suppression, opposite to the "transition" period.
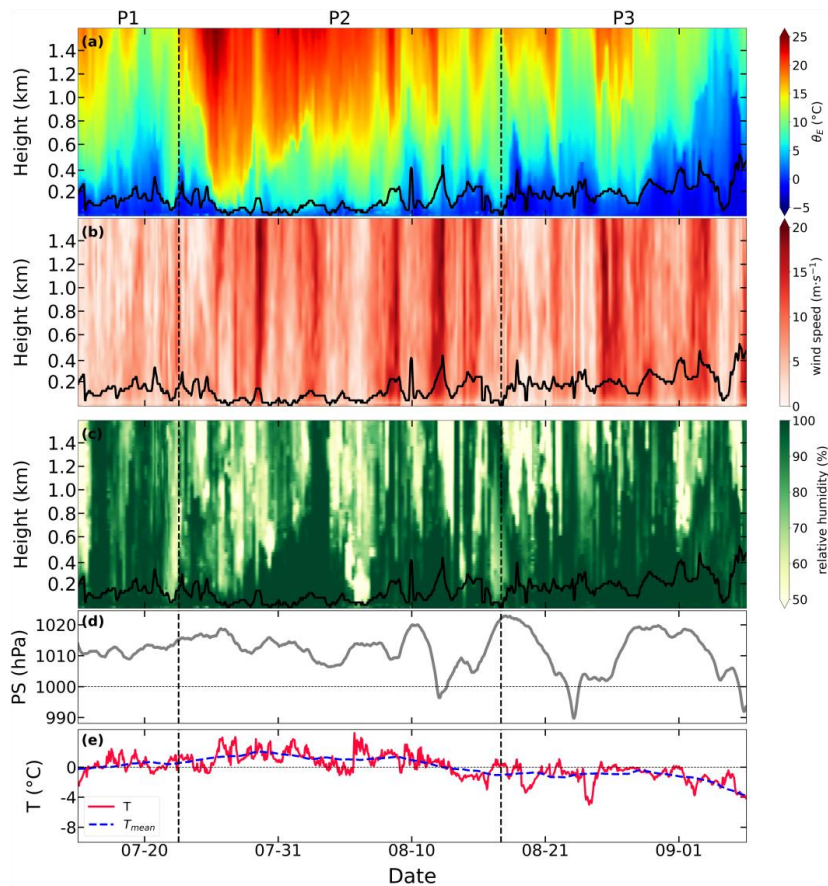
473

474   Figure 10 Similar to Fig. 9, but the period is from 15 July 2020 to 30 August 2020.

475

476   **5 Discussion**

477   The MOSAiC and SHEBA observations were both conducted over the Arctic sea ice. In terms

478   of the location of observation sites, the SHEBA campaign took place in the Beaufort and Chukchi

479   Seas (Perovich et al., 2003), while the MOSAiC observations took place in the higher latitudes of

480   the Fram Strait in June, July, and early August and near the North Pole in late August. The

481   comparison between the two campaigns could provide insight into the spatial and temporal

482   variability in the Arctic ABL structure. The monthly ABLHs of the two campaigns are presented in

483   Fig. 11a. We find that the overall distributions of ABLH are similar during the annual cycle, however,

484   the SHEBA ABLH is significantly higher than the MOSAiC ABLH in June and August. We will

485   discuss the differences based on the ABL thermal structure.

486   The comparisons of monthly θ_E profiles between the two campaigns during June and August

487   are presented in Fig. 11 (b, c). It is clear that θ_E within the ABL during the MOSAiC experiment is

488   much higher than that during the SHEBA experiment, especially in August. In June, the near-surface

489   θ_E values in both campaigns are close, because both were over melting sea ice. However, the upper-

490   layer θ_E during SHEBA is lower than that during MOSAiC, especially at a height of around 200 m,

491   which results in different low-level stabilities that affect the ABL development. This difference also

492   explains why the monthly SHEBA ABLH rises from May to June, but the monthly MOSAiC ABLH

493   decreases at this time. In July at SHEBA, the increased air temperature in the lower troposphere

494   combined with constrained near-surface θ_E results in a significant temperature inversion that

495   suppresses the ABL development (not shown). Thus, the ABLH values at SHEBA and MOSAiC are

496   comparable in July. In August, the θ_E profiles from the two campaigns are significantly different.

497   The lower troposphere at SHEBA starts to cool, with the SHEBA θ_E profile exhibiting a near-neutral

498   or convective state, while the MOSAiC θ_E profile shows a further enhanced surface temperature

499   inversion, which maintains the ABL suppression. To sum up, the increase in air temperature in the

500   lower troposphere in early summer during MOSAiC precedes that during SHEBA, while the cooling

501   of the lower troposphere in late summer during MOSAiC lags that during SHEBA. These are the

502   main factors contributing to the ABLH differences between the two campaigns.

503   The atmospheric warming during the MOSAiC summer is most likely attributed to different

504   surface conditions and different synoptic backgrounds. During June–July and early August at

505   MOSAiC, the observations were made much closer to the ice edge than the observations during

506   SHEBA, which might impact the air temperature across the ABL. Additionally, these two campaigns

507   were in different storm tracks with markedly different types of regional advection patterns. Synoptic

508   variability likely plays a big role in the ABL thermal structure. In summary, there is large variability

509   in the Arctic ABL structure during summer caused by the surface melting state, and more detailed

510   assessments are needed to study the specific causes for the atmospheric warming and possible

511   influences of changing Arctic conditions on the ABL structure.
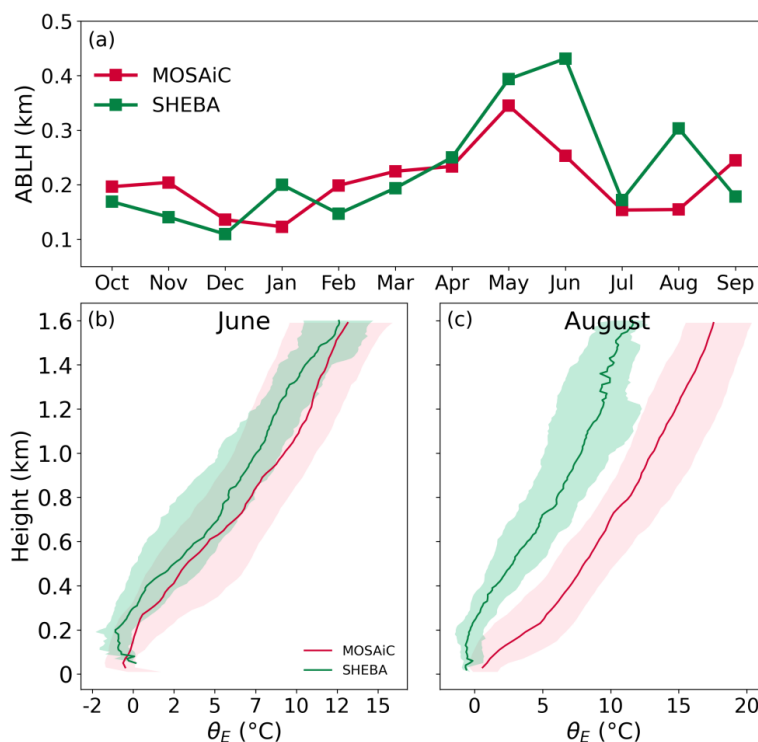
512

513   Figure 11 Comparison of ABL during the SHEBA (green squares, lines, and shadings) and the

514   MOSAiC (red squares, lines, and shadings) observation, including (a) annual cycle of median

515   ABLH and Monthly θ_E profiles in (b) June and (c) August. The solid lines in (b–c) indicate the

516   median profiles, and the shadings indicate the range of 25- and 75- percentile profiles.

517

518   **6 Conclusions**

23

519   This study is carried out using radiosounding data and corresponding surface meteorological

520   observations collected during the MOSAiC expedition, with high temporal resolution and a year-

521   round period. Based on these profiles, a full-year evolution of ABLH is derived using the Ri_b

522   algorithm with the optimal Ri_{bc} of 0.15. Subsequently, we analyze the characteristics and evolution

523   of ABLHs during the MOSAiC period, and the related controlling factors, including the ABL

524   thermal structure and near-surface conditions. Lastly, we use two cases to explore the mechanisms

525   of ABL development and suppression over the Arctic sea-ice surface. The main conclusions are as

526   follows.

527   During the MOSAiC year, the number of SBL samples is more than that of CBL samples,

528   accounting for 72 % and 28 %, respectively. The median SBL and CBL heights are 148 m and 362

529   m, respectively. The annual cycle of the Arctic ABLH is clearly characterized by a distinct peak in

530   May and an abrupt decrease in the following July and August, with a second minimum in December

531   and January. Compared to the SHEBA ABLH, the MOSAiC ABLH is suppressed in June and August,

532   which is caused by the increase atmospheric warming in the MOSAiC ABL during the "summer

533   melt" period compared to SHEBA.

534   The annual cycle of ABLH over the Arctic Ocean is primarily controlled by the seasonal

535   evolution of the ABL thermal structure and near-surface meteorological conditions. In the "winter"

536   period, temperature inversions form due to negative net radiation at the surface and are associated

537   with low ABLHs. In the "transition" period, the rapid increase of near-surface temperature weakens

538   the temperature inversion, facilitating the development of the ABL. In the "summer melt" period,

539   temperature inversions are generated by surface melt and warm-air advection and they suppress the

540   ABL development. For near-surface conditions, the temperature gradient is anti-correlated with the

541   ABLH, and a negative temperature gradient is necessary for ABL development. In addition, the

542   friction velocity is significantly correlated with the ABLH, related to the contributions of wind shear

543   to the ABL development. Significant correlation between the TKE dissipation rate and the ABLH

544   indicates that ABL development generally corresponds with intensive turbulence near the surface.

545   During MOSAiC, the development of the ABL is irregular, and only occurs during a few

546   periods. The year is characterized by occasions of abrupt growth of the ABLH and intensive ABLH

547   variation for several days thereafter. These unique features are caused by large-scale synoptic

548   processes (e.g., advection events). It is worth noting that some large-scale events can have the

549 opposite effects on the ABL in different periods. For example, warm-air advection can facilitate

550 ABL development in the "transition" period but can cause ABL suppression in the "summer melt"

551 period, which is because the constrained near-surface temperature cannot be changed by the warm

552 advection.

553   The findings reported above are helpful to understand the full-year ABL features over the

554 central Arctic Ocean in the 'new Arctic' period from the perspective of ABLH. The ABLH contains

555 information directly related to the thermal structure of the ABL and captures the impacts of weather

556 events and large-scale circulations on the ABL structure. Coupling between the cloud mixed layer

557 and surface mixed layer could also be recognized by the Ri_b algorithm and influenced the ABLH

558 variation, which is similar to Brooks et al. (2017). However, the representativity of these results

559 must still be established by comparing them with additional observations, and the influences of other

560 variables (e.g., energy budget terms) on the ABLH should also be considered in future research.

561

Data Availability

563 The   radiosonde   data   are   available   at   the   PANGAEA   Data   Publisher   at

564 https://doi.org/10.1594/PANGAEA.928656 (Maturilli et al., 2021). All value-added products and

565 surface meteorological data are archived in the US Department of Energy Atmospheric Radiation

566 Measurement Program. The Planetary Boundary Layer Height Value-Added Product is available at

567 http://dx.doi.org/10.5439/1150253 (Riihimaki et al., 2019). The Interpolated sounding value-added

568 product is available at http://dx.doi.org/10.5439/1095316 (Jensen et al., 2019). The MOSAiC

569 surface flux and other meteorological data are available at the Arctic Data Center at

570 http://dx.doi.org/10.18739/A2PV6B83F (Cox et al., 2023).

571

Competing interests

573 The contact author has declared that none of the authors has any competing interests.

574

584

594 **References**

595 Andreas, E. L., Claffy, K. J., and Makshtas, A. P.: Low-level atmospheric jets and inversions over
596   the western Weddell Sea, Boundary Layer Meteorol., 97, 459-486,
597   https://doi.org/10.1023/A:1002793831076, 2000.

598 Banta, R. M., Pichugina, Y. L., and Newsom, R. K.: Relationship between low-level jet properties
599   and turbulence kinetic energy in the nocturnal stable boundary layer, J. Atmos. Sci., 60, 2549-
600   2555, https://doi.org/10.1175/1520-0469(2003)060<2549:RBLJPA>2.0.CO;2, 2003.

601 Blunden, J. and Arndt, D. S.: A Look at 2018: Takeaway Points from the State of the Climate
602   Supplement, Bull. Amer. Meteorol. Soc., 100, 1625-1636, https://doi.org/10.1175/bams-d-19-
603   0193.1, 2019.

604 Brooks, I. M., Tjernstrom, M., Persson, P. O. G., Shupe, M. D., Atkinson, R. A., Canut, G., Birch,
605   C. E., Mauritsen, T., Sedlar, J., and Brooks, B. J.: The Turbulent Structure of the Arctic
606   Summer Boundary Layer During The Arctic Summer Cloud-Ocean Study, J. Geophys. Res.-
607   Atmos., 122, 9685-9704, https://doi.org/10.1002/2017jd027234, 2017.

608 Busch, N., Ebel, U., Kraus, H., and Schaller, E.: The structure of the subpolar inversion-capped
609   ABL, Archives for meteorology, geophysics, and bioclimatology, Series A, 31, 1-18,
610   https://doi.org/10.1007/BF02257738, 1982.

611 Dai, C., Gao, Z., Wang, Q., and Cheng, G.: Analysis of Atmospheric Boundary Layer Height
612   Characteristics over the Arctic Ocean Using the Aircraft and GPS Soundings, Atmospheric
613   Ocean. Sci., 4, 124-130, https://doi.org/10.1080/16742834.2011.11446916, 2011.

614 Cox, C., Gallagher, M., Shupe, M., Persson, O., Blomquist, B., Grachev, A., Riihimaki, L.,
615   Kutchenreiter, M., Morris, V., Solomon, A., Brooks, I., Costa, D., Gottas, D., Hutchings, J.,
616   Osborn, J., Morris, S., Preusser, A., Uttal, T.: Met City meteorological and surface flux
617   measurements (Level 3 Final), Multidisciplinary drifting Observatory for the Study of Arctic
618   Climate (MOSAiC), central Artic, October 2019 - September 2020 [data set],
619   https://doi.org/10.18739/A2PV6B83F, 2023.

620 Dai, C., Wang, Q., Kalogiros, J. A., Lenschow, D. H., Gao, Z., and Zhou, M.: Determining
621   Boundary-Layer Height from Aircraft Measurements, Boundary Layer Meteorol., 152, 277-
622   302, https://doi.org/10.1007/s10546-014-9929-z, 2014.

623 Deardorff, J. W.: Parameterization of the Planetary Boundary layer for Use in General Circulation
624   Models, Mon. Weather Rev., 100, 93-106, https://doi.org/10.1175/1520-

625   0493(1972)100<0093:Potpbl>2.3.Co;2, 1972.

626 Francis, J. A. and Hunter, E.: New insight into the disappearing Arctic sea ice, EOS Trans. Am.
627   Geophys. Union, 87, 509-511, https://doi.org/10.1029/2006EO460001, 2006.

628 Gao, Z., Chae, N., Kim, J., Hong, J., Choi, T., and Lee, H.: Modeling of surface energy partitioning,
629   surface temperature, and soil wetness in the Tibetan prairie using the Simple Biosphere Model
630   2 (SiB2), J. Geophys. Res.-Atmos., 109, https://doi.org/10.1029/2003JD004089, 2004.

631 Graversen, R. G., Mauritsen, T., Tjernstrom, M., Kallen, E., and Svensson, G.: Vertical structure of
632   recent Arctic warming, Nature, 451, 53-U54, https://doi.org/10.1038/nature06502, 2008.

633 Hartfield, G., Blunden, J., and Arndt, D. S.: State of the Climate in 2017, Bull. Amer. Meteorol.
634   Soc., 99, Si-S310, https://doi.org/10.1175/2018BAMSStateoftheClimate.1, 2018.

635 Heffter, J. L.: Transport layer depth calculations., Second Joint Conference on Applications of Air
636   Pollution Meteorology, 1980.

637 Holtslag, A. A. M. and Nieuwstadt, F. T. M.: Scaling the atmospheric boundary layer, Boundary
638   Layer Meteorol., 36, 201-209, https://doi.org/10.1007/BF00117468, 1986.

639 Jens Havskov, S., Alix, R., Thomas, E., and Erik, L.: Mesoscale influence on long-range transport
640   — evidence from ETEX modelling and observations, Atmos. Environ., 32, 4207-4217,
641   https://doi.org/10.1016/S1352-2310(98)00183-6, 1998.

642 Jensen, M., Giangrande, S., Fairless, T., and Zhou, A.: Interpolated Sonde
643   (INTERPOLATEDSONDE), Atmospheric Radiation Measurement (ARM) User Facility [data
644   set], https://doi.org/10.5439/1095316, 2019.

645 Jozef, G., Cassano, J., Dahlke, S., and de Boer, G.: Testing the efficacy of atmospheric boundary
646   layer height detection algorithms using uncrewed aircraft system data from MOSAiC, Atmos.
647   Meas. Tech., 15, 4001-4022, https://doi.org/10.5194/amt-15-4001-2022, 2022.

648 Knudsen, E. M., Heinold, B., Dahlke, S., Bozem, H., Crewell, S., Gorodetskaya, I. V., Heygster, G.,
649   Kunkel, D., Maturilli, M., Mech, M., Viceto, C., Rinke, A., Schmithusen, H., Ehrlich, A.,
650   Macke, A., Luepkes, C., and Wendisch, M.: Meteorological conditions during the
651   ACLOUD/PASCAL field campaign near Svalbard in early summer 2017, Atmospheric Chem.
652   Phys., 18, 17995-18022, https://doi.org/10.5194/acp-18-17995-2018, 2018.

653 Knust, R.: Polar Research and Supply Vessel POLARSTERN operated by the Alfred-Wegener-
654   Institute, Journal of large-scale research facilities JLSRF, 3, https://doi.org/10.17815/jlsrf-3-
655   163, 2017.

656 Konor, C. S., Boezio, G. C., Mechoso, C. R., and Arakawa, A.: Parameterization of PBL Processes
657   in an Atmospheric General Circulation Model: Description and Preliminary Assessment, Mon.
658   Weather Rev., 137, 1061-1082, https://doi.org/10.1175/2008mwr2464.1, 2009.

659 Kwok, R.: Arctic sea ice thickness, volume, and multiyear ice coverage: losses and coupled
660   variability (1958–2018), Environ. Res. Lett., 13, https://doi.org/10.1088/1748-9326/aae3ec,
661   2018.

662 Landrum, L. and Holland, M. M.: Extremes become routine in an emerging new Arctic, Nature
663   Clim. Change, 10, 1108-1115, https://doi.org/10.1038/s41558-020-0892-z, 2020.

664 Liang, X.-Z. and Liu, S.: Observed Diurnal Cycle Climatology of Planetary Boundary Layer Height,
665   J. Clim., 23, 5790-5809, https://doi.org/10.1175/2010jcli3552.1, 2010.

666 Mahrt, L.: Modelling the depth of the stable boundary-layer, Boundary Layer Meteorol., 21, 3-19,
667   https://doi.org/10.1007/BF00119363, 1981.

668 Marsik, F. J., Fischer, K. W., McDonald, T. D., and Samson, P. J.: Comparison of Methods for
669   Estimating Mixing Height Used during the 1992 Atlanta Field Intensive, J. Appl. Meteorol.
670   Climatol.,   34,   1802-1814,   https://doi.org/10.1175/1520-
671   0450(1995)034<1802:Comfem>2.0.Co;2, 1995.

672 Maturilli, M., Holdridge, D. J., Dahlke, S., Graeser, J., Sommerfeld, A., Jaiser, R., Deckelmann, H.,
673   and Schulz, A.: Initial radiosonde data from 2019-10 to 2020-09 during project MOSAiC,
674   PANGAEA [data set], https://doi.org/10.1594/PANGAEA.928656, 2021.

675 Nixdorf, U., Dethloff, K., Rex, M., Shupe, M., Sommerfeld, A., Perovich, D. K., Nicolaus, M.,
676   Heuze, C., Rabe, B., Loose, B., Damm, E., Gradinger, R., Fong, A., Maslowski, W., Rinke, A.,
677   Kwok, R., Spreen, G., Wendisch, M., Herber, A., Hirsekorn, M., Mohaupt, V., Frickenhaus,
678   S., Immerz, A., Weiss-Tuider, K., Koenig, B., Mengedoht, D., Regnery, J., Gerchow, P.,
679   Ransby, D., Krumpen, T., Morgenstern, A., Haas, C., Kanzow, T., Rack, F., Saitzev, V.,
680   Sokolov, V., Makarov, A., Schwarze, S., Wunderlick, T., Wurr, K., Boetius, A.: MOSAiC
681   extended acknowledgement., Zenodo., http://dx.doi.org/10.5281/zenodo.5541624, 2021.

682 Overland, J. E., Dunlea, E. J., Box, J. E., Corell, R. W., Forsius, M., Kattsov, V. M., Olsen, M. S.,
683   Pawlak, J., Reiersen, L. O., and Wang, M.: The urgency of Arctic change, Polar Sci., 21, 6-13,
684   https://doi.org/10.1016/j.polar.2018.11.008, 2019.

685 Palo, T., Vihma, T., Jaagus, J., and Jakobson, E.: Observations of temperature inversions over
686   central Arctic sea ice in summer, Q. J. R. Meteorol. Soc., 143, 2741-2754,
687   https://doi.org/10.1002/qj.3123, 2017.

688 Perovich, D. K., Grenfell, T. C., Richter-Menge, J. A., Light, B., Tucker III, W. B., and Eicken, H.:
689   Thin and thinner: Sea ice mass balance measurements during SHEBA, J. Geophys. Res.-
690   Oceans, 108, https://doi.org/10.1029/2001JC001079, 2003.

691 Persson, P. O. G., Fairall, C. W., Andreas, E. L., Guest, P. S., and Perovich, D. K.: Measurements
692   near the Atmospheric Surface Flux Group tower at SHEBA: Near-surface conditions and
693   surface energy budget, J. Geophys. Res.-Oceans, 107, 35,
694   https://doi.org/10.1029/2000jc000705, 2002.

695 Richardson, H., Basu, S., and Holtslag, A. A. M.: Improving Stable Boundary-Layer Height
696   Estimation Using a Stability-Dependent Critical Bulk Richardson Number, Boundary Layer
697   Meteorol., 148, 93-109, https://doi.org/10.1007/s10546-013-9812-3, 2013.

698 Riihimaki, L., Sivaraman, C., and Zhang, D.: Planetary Boundary Layer Height
699   (PBLHTSONDE1MCFARL), Atmospheric Radiation Measurement (ARM) User Facility
700   [data set], https://doi.org/10.5439/1150253, 2019.

701 Seibert, P., Beyrich, F., Gryning, S. E., Joffre, S., Rasmussen, A., and Tercier, P.: Review and
702   intercomparison of operational methods for the determination of the mixing height, Atmos.
703   Environ., 34, 1001-1027, https://doi.org/10.1016/s1352-2310(99)00349-0, 2000.

704   Seidel, D. J., Ao, C. O., and Li, K.: Estimating climatological planetary boundary layer heights from
705   radiosonde observations: Comparison of methods and uncertainty analysis, J. Geophys. Res.-
706   Atmos., 115, https://doi.org/10.1029/2009JD013680, 2010.

707   Seidel, D. J., Zhang, Y. H., Beljaars, A., Golaz, J. C., Jacobson, A. R., and Medeiros, B.:
708   Climatology of the planetary boundary layer over the continental United States and Europe, J.
709   Geophys. Res.-Atmos., 117, 15, https://doi.org/10.1029/2012jd018143, 2012.

710   Shupe, M. D., Persson, P. O. G., Brooks, I. M., Tjernstrom, M., Sedlar, J., Mauritsen, T., Sjogren,
711   S., and Leck, C.: Cloud and boundary layer interactions over the Arctic sea ice in late summer,
712   Atmos. Chem. Phys., 13, 9379-9399, https://doi.org/10.5194/acp-13-9379-2013, 2013.

713   Shupe, M. D., Rex, M., Blomquist, B., Persson, P. O. G., Schmale, J., Uttal, T., Althausen, D.,
714   Angot, H., Archer, S., Bariteau, L., Beck, I., Bilberry, J., Bucci, S., Buck, C., Boyer, M.,
715   Brasseur, Z., Brooks, I. M., Calmer, R., Cassano, J., Castro, V., Chu, D., Costa, D., Cox, C. J.,
716   Creamean, J., Crewell, S., Dahlke, S., Damm, E., de Boer, G., Deckelmann, H., Dethloff, K.,
717   Dütsch, M., Ebell, K., Ehrlich, A., Ellis, J., Engelmann, R., Fong, A. A., Frey, M. M., Gallagher,
718   M. R., Ganzeveld, L., Gradinger, R., Graeser, J., Greenamyer, V., Griesche, H., Griffiths, S.,
719   Hamilton, J., Heinemann, G., Helmig, D., Herber, A., Heuzé, C., Hofer, J., Houchens, T.,
720   Howard, D., Inoue, J., Jacobi, H.-W., Jaiser, R., Jokinen, T., Jourdan, O., Jozef, G., King, W.,
721   Kirchgaessner, A., Klingebiel, M., Krassovski, M., Krumpen, T., Lampert, A., Landing, W.,
722   Laurila, T., Lawrence, D., Lonardi, M., Loose, B., Lüpkes, C., Maahn, M., Macke, A.,
723   Maslowski, W., Marsay, C., Maturilli, M., Mech, M., Morris, S., Moser, M., Nicolaus, M.,
724   Ortega, P., Osborn, J., Pätzold, F., Perovich, D. K., Petäjä, T., Pilz, C., Pirazzini, R., Posman,
725   K., Powers, H., Pratt, K. A., Preußer, A., Quéléver, L., Radenz, M., Rabe, B., Rinke, A., Sachs,
726   T., Schulz, A., Siebert, H., Silva, T., Solomon, A., Sommerfeld, A., Spreen, G., Stephens, M.,
727   Stohl, A., Svensson, G., Uin, J., Viegas, J., Voigt, C., von der Gathen, P., Wehner, B., Welker,
728   J. M., Wendisch, M., Werner, M., Xie, Z., and Yue, F.: Overview of the MOSAiC expedition—
729   Atmosphere, Elementa: Sci. Anthrop., 10, https://doi.org/10.1525/elementa.2021.00060, 2022.

730   Snyder, B. J. and Strawbridge, K. B.: Meteorological analysis of the Pacific 2001 air quality field
731   study, Atmos. Environ., 38, 5733-5743, https://doi.org/10.1016/j.atmosenv.2004.02.068, 2004.

732   Solomon, A., Shupe, M. D., Persson, P. O. G., and Morrison, H.: Moisture and dynamical
733   interactions maintaining decoupled Arctic mixed-phase stratocumulus in the presence of a
734   humidity inversion, Atmos. Chem. Phys., 11, 10127-10148, https://doi.org/10.5194/acp-11-
735   10127-2011, 2011.

736   Sotiropoulou, G., Sedlar, J., Tjernström, M., Shupe, M. D., Brooks, I. M., and Persson, P. O. G.:
737   The thermodynamic structure of summer Arctic stratocumulus and the dynamic coupling to the
738   surface, Atmos. Chem. Phys., 14, 12573-12592, https://doi.org/10.5194/acp-14-12573-2014,
739   2014.

740   Stull, R. B.: An Introduction to Boundary Layer Meteorology, ISBN 1383-8601, 1988.

741   Suarez, M. J., Arakawa, A., and Randall, D. A.: The Parameterization Of the Planetary Boundary
742   Layer in the UCLA General Circulation Model: Formulation and Results, Mon. Weather Rev.,
743   111, 2224-2243, https://doi.org/10.1175/1520-0493(1983)111<2224:Tpotpb>2.0.Co;2, 1983.

744   Tjernström, M.: Is There a Diurnal Cycle in the Summer Cloud-Capped Arctic Boundary Layer?, J.

745   Atmos. Sci., 64(11), 3970-3986, https://doi.org/10.1175/2007JAS2257.1, 2007.

746 Tjernström, M., Balsley, B. B., Svensson, G., and Nappo, C. J.: The Effects of Critical Layers on
747   Residual Layer Turbulence, J. Atmos. Sci., 66, 468-480,
748   https://doi.org/10.1175/2008jas2729.1, 2009.

749 Tjernström, M., Birch, C. E., Brooks, I. M., Shupe, M. D., Persson, P. O. G., Sedlar, J., Mauritsen,
750   T., Leck, C., Paatero, J., Szczodrak, M., and Wheeler, C. R.: Meteorological conditions in the
751   central Arctic summer during the Arctic Summer Cloud Ocean Study (ASCOS), Atmos. Chem.
752   and Phys., 12, 6863-6889, https://doi.org/10.5194/acp-12-6863-2012, 2012.

753 Tjernström, M. and Graversen, R. G.: The vertical structure of the lower Arctic troposphere analysed
754   from observations and the ERA-40 reanalysis, Q. J. R. Meteorol. Soc., 135, 431-443,
755   https://doi.org/10.1002/qj.380, 2009.

756 Uttal, T., Curry, J. A., McPhee, M. G., Perovich, D. K., Moritz, R. E., Maslanik, J. A., Guest, P. S.,
757   Stern, H. L., Moore, J. A., Turenne, R., Heiberg, A., Serreze, M. C., Wylie, D. P., Persson, O.
758   G., Paulson, C. A., Halle, C., Morison, J. H., Wheeler, P. A., Makshtas, A., Welch, H., Shupe,
759   M. D., Intrieri, J. M., Stamnes, K., Lindsey, R. W., Pinkel, R., Pegau, W. S., Stanton, T. P.,
760   and Grenfeld, T. C.: Surface Heat Budget of the Arctic Ocean, Bull. Amer. Meteorol. Soc., 83,
761   255-276, https://doi.org/10.1175/1520-0477(2002)083<0255:Shbota>2.3.Co;2, 2002.

762 Vihma, T.: Effects of Arctic Sea Ice Decline on Weather and Climate: A Review, Surv. Geophys.,
763   35, 1175-1214, https://doi.org/10.1007/s10712-014-9284-0, 2014.

764 Vihma, T., Kilpelainen, T., Manninen, M., Sjoblom, A., Jakobson, E., Palo, T., Jaagus, J., and
765   Maturilli, M.: Characteristics of Temperature and Humidity Inversions and Low-Level Jets
766   over Svalbard Fjords in Spring, Adv. Meteorol., 2011, 14,
767   https://doi.org/10.1155/2011/486807, 2011.

768 Vogelezang, D. H. P. and Holtslag, A. A. M.: Evaluation and model impacts of alternative boundary-
769   layer height formulations, Boundary Layer Meteorol., 81, 245-269,
770   https://doi.org/10.1007/BF02430331, 1996.

771 Vullers, J., Achtert, P., Brooks, I. M., Tjernstrom, M., Prytherch, J., Burzik, A., and Neely, R.:
772   Meteorological and cloud conditions during the Arctic Ocean 2018 expedition, Atmos. Chem.
773   and Phys., 21, 289-314, https://doi.org/10.5194/acp-21-289-2021, 2021.

774 Wang, S., Wang, Q., Jordan, R. E., and Persson, P. O. G.: Interactions among longwave radiation
775   of clouds, turbulence, and snow surface temperature in the Arctic: A model sensitivity study,
776   J. Geophys. Res.-Atmos., 106, 15323-15333, https://doi.org/10.1029/2000JD900358, 2001.

777 Wetzel, C. and Bruemmer, B.: An Arctic inversion climatology based on the European Centre
778   Reanalysis ERA-40, Meteorologische Zeitschrift, 20, 589-600, https://doi.org/10.1127/0941-
779   2948/2011/0295, 2011.

780 Zhang, J. A., Rogers, R. F., Nolan, D. S., and Marks, F. D.: On the Characteristic Height Scales of
781   the Hurricane Boundary Layer, Mon. Weather Rev., 139, 2523-2535,
782   https://doi.org/10.1175/mwr-d-10-05017.1, 2011.

783 Zhang, Y., Gao, Z., Li, D., Li, Y., Zhang, N., Zhao, X., and Chen, J.: On the computation of
784   planetary boundary-layer height using the bulk Richardson number method, Geosci. Model

785   Dev., 7, 2599-2611, https://doi.org/10.5194/gmd-7-2599-2014, 2014.

786